Taylor & Francis
Taylor & Francis Group

Materials Science and Technology

ISSN: (Print) (Online) Journal homepage: https://www.tandfonline.com/loi/ymst20

# Eutectic composition titanium metal matrix composites for laser powder bed fusion via surface remelt analyses

**William R. Hixson, Junyang Yu, Alison Wilson, Howard J. Stone, Dieter Isheim & James Coakley**

**To cite this article:** William R. Hixson, Junyang Yu, Alison Wilson, Howard J. Stone, Dieter Isheim & James Coakley (2023): Eutectic composition titanium metal matrix composites for laser powder bed fusion via surface remelt analyses, Materials Science and Technology, DOI: 10.1080/02670836.2023.2178178

**To link to this article:** https://doi.org/10.1080/02670836.2023.2178178



Published online: 02 Mar 2023.

MATERIALS SCIENCE AND TECHNOLOGY
https://doi.org/10.1080/02670836.2023.2178178

I·M3 Institute of Materials, Minerals & Mining
Taylor & Francis Taylor & Francis Group



# Eutectic composition titanium metal matrix composites for laser powder bed fusion via surface remelt analyses

William R. Hixson[a], Junyang Yu[a], Alison Wilson[b], Howard J. Stone[b], Dieter Isheim[c,d] and James Coakley [a]

[a]Department of Mechanical and Aerospace Engineering, University of Miami, Coral Gables, FL, USA; [b]Department of Materials Science and Metallurgy, University of Cambridge, Cambridge, UK; [c]Department of Materials Science and Engineering, Northwestern University, Evanston, IL, USA; [d]Northwestern University Center for Atom-Probe Tomography (NUCAPT), Evanston, IL, USA

**ABSTRACT**

Ti-based metal matrix composites (MMCs) represent a material class with highly desired performance for the aerospace industry, but implementation has been hindered by poor processability. It is now being realised that MMCs can be formed *in situ* through the exploitation of rapid cooling rates of laser powder bed fusion, and targeting invariant reaction compositions to minimise the propensity for solidification cracking. We perform laser line scans and surface remelts of arc-melted Ti–0.38C, Ti–1.67B, Ti–8.5Si and Ti–32.5Fe wt-% eutectic compositions to assess potential material amenability to the laser powder bed fusion (LPBF) process at low cost as well as determining the nanostructure and hardness properties. The results indicate that MMCs are amenable to LPBF and may outperform conventional alloys.

**ARTICLE HISTORY**
Received 7 July 2022
Accepted 30 January 2023

**KEYWORDS**
Laser powder bed fusion; titanium; metal matrix composites; atom probe tomography; solidification

## Introduction

Ti based metal matrix composites (MMCs) are regarded as being among the most promising materials for enabling new aerospace systems, for example Ti–Si-based MMCs possess over double the specific strength and specific stiffness of conventional alloys [1]. It has been proposed that low-cost MMC microstructures can be formed *in situ* through co-solidification of a ceramic or intermetallic phase with a metal phase [1], and it is anticipated that these *in situ* MMCs will provide performance improvements over metallic and non-metallic materials [1].

Vardiman and Kant determined greatly enhanced fatigue properties in C and N ion implanted Ti6Al4V due to the formation of nanoscale TiC and TiN particles, thereby demonstrating the potential of Ti MMCs [2]. However, the implementation of MMCs has been limited by poor processability [3]. It is now recognised that laser powder bed fusion (LPBF) may offer a pathway to overcome this limitation and achieve complex MMC components by near net-shaping [4, 5]. Promising research regarding Ti-based MMC fabricability via LPBF has been performed but development in this area has been limited by powder feedstock quality and supply [4, 6–16]. Numerous authors have demonstrated enhanced mechanical properties of Ti and Ti6Al4V reinforced by TiC/TiB through LPBF utilising gas–liquid reaction [11], powder mixing [6, 13] or mechanically alloyed powder [8, 10, 17, 18]. Gussone et al. have previously utilised elemental blends to manufacture crack-free samples of eutectic Ti–32.5Fe wt-% via LPBF [9]. It is noteworthy that the base plate was heated to 600°C, a processing step that can be introduced to reduce hot-cracking, and the O content correspondingly increased to ~0.45 wt-%. The increase in O content resulted in extensive precipitation of large $\eta$-$Ti_4Fe_2O_x$ precipitates which will significantly influence properties. Ti–Si–C composites have been LPBF manufactured from mixes of Ti and SiC powders utilising a molar ratio of SiC:Ti = 1:1.95. This ratio resulted in precipitation of multiple ceramic and intermetallic phases [19]. To the authors' knowledge, a study targeting eutectic compositions has not been performed to date and Ti–Si MMCs remain unexplored.

Powder availability has remained the primary obstacle to experimental SLM alloy development, where it is impractical and costly to produce small-scale powder batch for preliminary trial compositions of interest [20]. He et al. demonstrated the powder-free experimental methodology to identify Ti6Al4V-*x*B compositions suitable for SLM processing. A wide composition range from 0 to 10 wt-% B additions were analysed and it was suggested that LPBF may be capable of fabricating such MMCs. The Ti6Al4V–*x*B candidate compositions were produced by first fabricating arc-melted buttons, which are much easier to produce than lab-scale powder batch, especially for a series of commercially unavailable compositions. The applicability of the powder-free methodology to material development was supported by evaluation of single-track melt

**CONTACT** James Coakley jcoakley@miami.edu Department of Mechanical and Aerospace Engineering, University of Miami, Coral Gables, FL 33146, USA

**Table 1.** Nominal and measured eutectic (1 – 5) and hyper-eutectic (6) compositions of the alloys manufactured.

| | Composition | | Hardness | |
|---|---|---|---|---|
| | Nominal (wt-%/at.-%) | Measured (wt-%/at.-%) | Arc-melted (Hv) | LPBF (Hv) |
| 1 | 100Ti/100Ti | – | 132 ± 2 | 174 ± 6 |
| 2 | Ti–0.38C/Ti–1.5C | Ti–0.38C/Ti–1.5C | 259 ± 10 | 456 ± 8 |
| 3 | Ti–1.67B/Ti–7.0B | Ti–1.62B/Ti–6.8B | 350 ± 30 | 464 ± 9 |
| 4 | Ti–8.5Si/Ti–13.7Si | Ti–8.47Si/Ti–13.63Si | 386 ± 21 | 684 ± 16 |
| 5 | Ti–32.5Fe/Ti–29.2Fe | Ti–31.4Fe/Ti–28.2Fe | 746 ± 26 | 769 ± 20 |
| 6 | Ti–15Si/Ti–23.1Si | Ti–14.92Si/Ti–23.0Si | 570 ± 80 | 619 ± 8 |

Note: C content was determined with an LECO gas analyser, Fe was determined by SEM-EDS, Si was determined by APT and EDS and B was determined by ICP-OES. The Vickers micro-hardness within the arc-melted and through the laser remelted regions are also presented.

pools made on solid Ti6Al4V and on one powder layer deposited over solid Ti6Al4V. A high level of similarity was observed between the former and the latter [20]. Further, in this study, full surface laser remelting was performed on the samples utilising a standard infill rastering pattern the sectioning of which shows a remelt-remelt overlap comparable to the meltpool patterning seen in multilayer builds.

Screening and assessment of Ti-based MMCs are warranted when one considers the exceptional mechanical properties and the existence of invariant reactions that can be exploited to close the solidification temperature range, minimising concerns associated with thermal cracking [21, 22] and porosity [23, 24] which ultimately limit LPBF candidate materials [25, 26]. In the current research, the amenabilty to LPBF and microstructure–micro-hardness relationships of four eutectic composition binary Ti alloys (nominal Ti–0.38C , Ti–1.7B , Ti–8.5Si and Ti–32.5Fe wt-%) are examined, and a hyper-eutectic Ti–15Si wt-% alloy is also presented for comparison. These compositions were selected to compare typical interstitial additions against substitutional additions, as well as to compare the role of increased alloying content across the eutectic compositions. As a first assessment in evaluating these compositions potential amenability to LPBF, arc-melted alloys were subject to single-line scan laser remelting as well as surface laser remelting as a means to simulate the initial microstructural development expected in LPBF. It is found that Ti–C, Ti–B and Ti–Si eutectic compositions are likely amenable to LPBF, and extensive hot-cracking was observed in Ti–32.5Fe wt-% surface remelts. All materials possessed high micro-hardness values and there were notable differences in the resultant nanostructures across compositions following laser remelting. The research is a further demonstration that extensive insight regarding alloy development for LPBF can be garnered from analysis of powder-free laser line-scan and surface remelt samples, where it is impractical to develop powder and perform extensive mechanical testing of every potential material of interest.

## Experimental details

### *Arc-melting and composition analysis*

High purity titanium sponge granules were arc-melted with TiC, $TiB_2$, Si or Fe to form 10 g button samples of pure Ti as well as nominal Ti–0.38C wt-%, Ti–1.67B wt-%, Ti–8.5Si wt-%, Ti–32.5Fe wt-% and Ti–15Si wt-% binary alloys, respectively. The nominal compositions were selected as approximate eutectic and hyper-eutectic compositions from the available literature [27–31]. The arc-melting chamber was evacuated to $10^{-5}$ mbar and back-filled with high purity Ar to 0.6 bar for melting. Each melted sample was flipped and remelted 10 times to improve homogeneity. C content was determined with an LECO gas analyser, and Si and Fe compositions were determined by scanning electron microscopy energy dispersive spectroscopy (SEM-EDS) utilising a Zeiss Ultra Plus with an EDAX Apollo 10 EDS detector. The local composition of Ti–15Si wt-% was also determined with a CAMECA LEAP 5000 XS atom probe tomograph (APT). B content was determined by inductively coupled plasma optical emission spectroscopy (ICP-OES). The nominal and measured compositions of each button sample are presented in Table 1, and the materials are referred to by the nominal composition throughout this article.

### *Laser melting, XRD and hardness testing*

The button samples were sectioned to produce multiple flat samples from each button. Localised melting by laser line scans was initially performed across a power range from 80 to 170 W with constant speed of 800 mm $s^{-1}$, utilising an EOS M100. Samples were further sectioned normal to the laser scan direction, mounted in resin and polished using standard metallographic protocols. G19 Kroll's reagent was applied to the polished surfaces for 20 s to obtain surface relief suitable for optical microscopy with a Keyence VHX microscope. Following preliminary assessment, the 80 and 140 W power line scans were selected for SEM analysis and presented herein, where in depth characterisation of all samples would be superfluous.

Full surface laser scans were performed on separate sections at 140 W/800 mm $s^{-1}$ laser energy and 30$\mu$m hatch-distance to simulate a full LPBF surface. 20 Vickers micro-hardness tests were performed across the surface remelted sections of each composition and within the arc-melted region utilising a Tukon microhardness tester to obtain statistically averaged hardness values. X-ray diffraction (XRD) was also performed with a Rigaku D-Max B at 20 keV/40 mA for bulk phase identification of the arc-melted samples and the laser surface melted samples.

The heat flow and meltpool fluid dynamics are naturally different between a surface laser remelt regime and a powder layer melting on built-up surface, but the laser remelting experiments are intended to be demonstrative as to the behaviour of the targeted compositions not authoritative as to successful scanning parameters. The single line scans were run with a 500-$\mu$m hatch spacing such that each laser melt was essentially thermally independent. The full surface scans employed a standard infill pattern with a 30-$\mu$m hatch spacing where every other hatch line was consecutively melted then the remaining alternating hatch lines were melted in immediate succession. With this infill pattern and the short time between the first and second laser passes, enough heat was retained to allow the second pass to melt deeper and wider than the first pass such that the cross section of the melt pools does not show evidence of the first pass due to complete overlap, Figure 2. The full surface melted specimens were sectioned normal to the laser melt pathway to expose the melt pool cross-sections; the same processing for imaging was done as for the single line scan specimens.

### APT

During the period of initial research regarding Ti–Si MMCs, a Ti–15Si wt-% material containing line scans was analysed by APT at the Northwestern University Center for Atom Probe Tomography (NUCAPT). APT samples were prepared by a standard lift-out, mounting of blanks on microtip arrays, and nanotip sharpening [32–34] employing an FEI Helios NanoLab 600 Dual-Beam focused ion-beam (FIB) microscope equipped with an Omniprobe Autoprobe 200 micromanipulator. APT was performed with UV (355 nm wavelength) laser pulsing at 30 K base temperature and 25 pJ laser pulse energy at a 4% detection rate. Data acquisition was interrupted after detecting over 150M atoms, which encompassed a representative volume of the cellular nanostructure. After data collection, runs were reconstructed and examined in three-dimensions (3-D) utilising CAMECA's IVAS 3.8 data analysis software program. Si isoconcentration surfaces were used to identify and visualise the cellular nanostructure. Proximity histogram concentration profiles (proxigrams) [32,35–39] were then created relative to the Si isoconcentration surfaces for quantitative compositional analysis.

## Results

### Composition and XRD measurements

The arc-melted alloy compositions were close to the targeted nominal composition, Table 1. Phase identification was performed by comparing the experimentally obtained XRD patterns to simulated patterns available on the materials database materialsproject.org [40], with peak positions identified in Figure 1. The Ti–0.38C wt-% material is composed of hexagonal close packed (HCP) $\alpha$-Ti ($P6_3/mmc$ [194]) and cubic TiC ($Fm\bar{3}m$ [225]), and this is consistent for both the arc-melted and laser remelt regions (Figure 1 a). Similar observations were made of the Ti–1.67B wt-% material, which is composed of $\alpha$-Ti and orthorhombic TiB (Pnma [62]) (Figure 1 b). It should be noted that $\alpha$ and $\alpha'$ possess the same crystal structure and are indistinguishable from each other in such XRD patterns.

The arc-melted Ti–32.5Fe appears to possess a predominantly $\alpha$-Ti + cubic TiFe ($Pm\bar{3}m$ [221]) microstructure (Figure 1 d). The XRD pattern from the laser surface remelt region is notably different, where the $(10\bar{1}1)$ $\alpha$ peak is not present, implying that the $\beta$ to $\alpha$ transformation has been suppressed by the rapid cooling rate of the laser remelt, i.e. the microstructure is $\beta$-Ti ($Im\bar{3}m$ [229]) + cubic TiFe. Reflections associated with orthorhombic $\alpha''$ martensite and $\omega$ phases are notably absent in the laser remelt diffraction pattern [41, 42].

The arc-melted Ti–8.5Si wt-% and Ti–15Si wt-% (red data points of Figure 1 (c) and (e) respectively) are composed of $\alpha$-Ti + hexagonal $Ti_5Si_3$ ($P6_3/mcm$ [193]), however, it is difficult to determine with this methodology if hexagonal $Ti_3Si$ ($P6_3/mmc$ [194]) is also present due to the extensive overlaying peak positions with $Ti_5Si_3$. We conclude that the arc-melted Ti–Si alloys are predominantly $\alpha$-Ti + $Ti_5Si_3$ from the distinct $Ti_5Si_3$ $(30\bar{3}0)$, $(3\bar{1}\bar{2}0)$ and $(2\bar{1}\bar{1}1)$ reflections, while noting that the XRD suggests a low volume fraction of $Ti_3Si$ within Ti–15Si wt-% from the minor peaks labelled $(20\bar{2}2)$ and $(303\bar{1})$ in Figure 1(e).

The XRD patterns from the laser remelt regions of eutectic Ti–8.5Si wt-% and hyper-eutectic Ti–15Si wt-% notably differ, black data points of Figure 1(c) and 1(e) respectively. Peak broadening obscures distinct peaks in the Ti–8.5Si wt-% sample, but in both diffraction patterns the $\alpha$ + $Ti_5Si_3$ phases are prominent.

### Microscopy and hardness testing

The melt pool geometries were qualitatively compared across compositions and laser energies (Figure 3); all

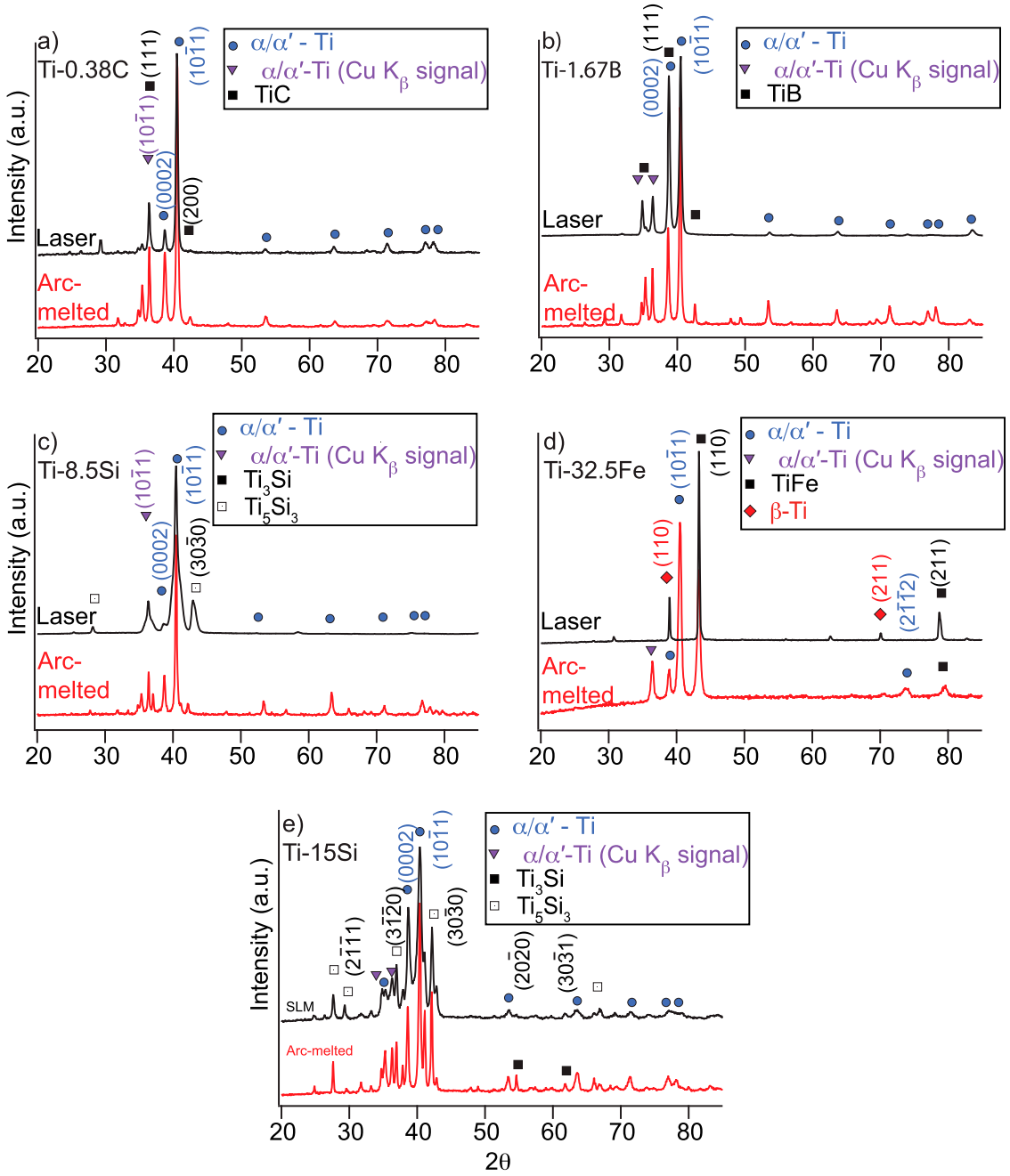


**Figure 1.** XRD spectra of the arc-melted button samples and laser remelt solidified surfaces for (a) Ti–0.38C wt-%, (b) Ti–1.67B wt-%, (c) Ti–8.5Si wt-%, (d) Ti–32.5Fe wt-%, (e) Ti–15Si wt-%.

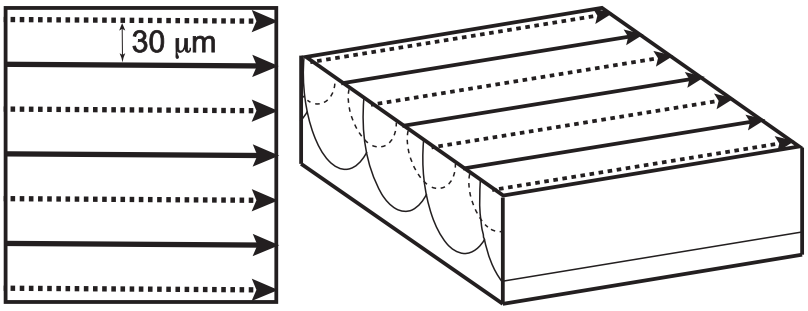


**Figure 2.** Schematic diagram showing the full surface remelting scan strategy: two passes are made with the laser at the same power for each pass. The laser first rasters along all of the dashed paths (with representative dashed meltpools) then immediately rasters along all of the solid paths (with representative final, solid line meltpools).

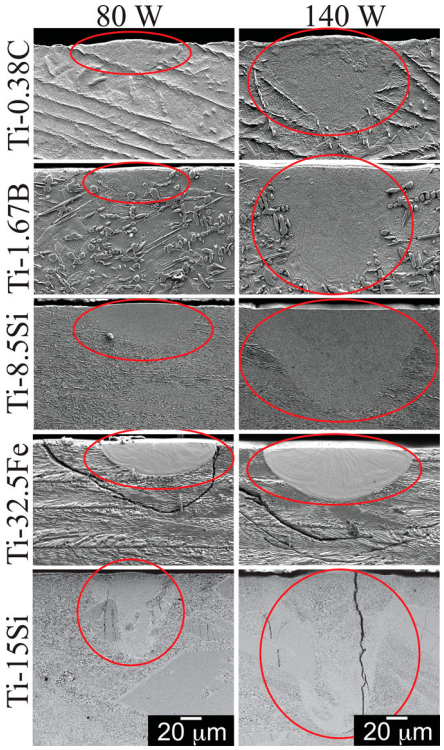


**Figure 3.** Secondary electron SEM images of the sectioned single line scans illustrating the line scan depth and shape (highlighted by a red oval) at different laser powers for the in-situ Ti-based MMCs examined. All images at matching magnification.

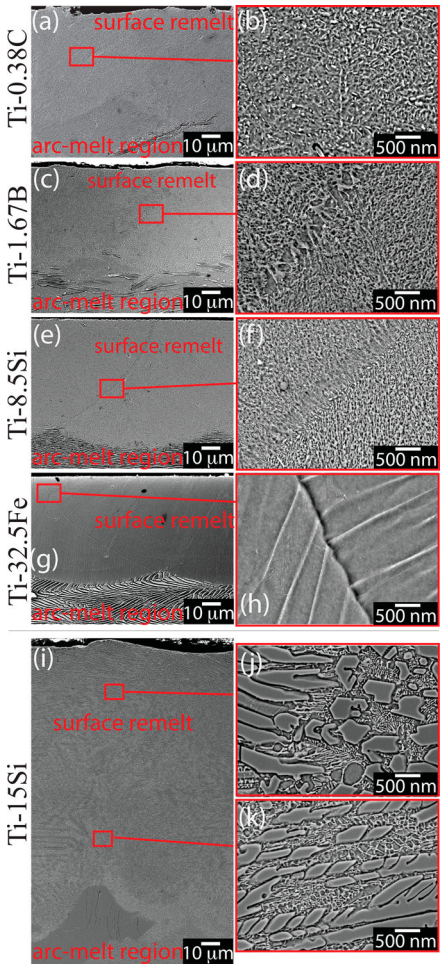


**Figure 4.** Secondary electron SEM images of the sectioned surface melted samples illustrating the effect of melt pool overlap.

sections for microscopy were cut normal to the laser pathway. For Ti–0.38C, Ti–1.67B and Ti–8.5Si compositions, the melt-pools were hemispherical to 100 W energy while Ti–32.5Fe exhibited shallow penetration depths to 170 W (Figure 3). Cracking was noted in the surrounding arc-melted region of all Ti–32.5Fe samples following single line scan laser remelt with the crack propagating along the lath structure interface, but cracking did not occur within the melt-pool itself, Figure 3. Vertical cracking was noted within Ti–15Si across all laser pulse energies. It was noted that large silicides in the arc-melted region also showed significant cracking following laser line scans, suggesting that crack initiation may occur in the arc-melted region (Figure 3).

The full surface laser remelt samples were sectioned and examined by SEM and exhibit overlapping regions of resolidification (Figure 4 ). The Ti–1.67B and Ti–8.5Si samples both exhibited a transition zone at the solidification boundaries of roughly 300 nm (Figure 4d and f ). The Ti–32.5Fe sample exhibited a sharp grain boundary interface (Figure 4 h). The Ti–0.38C and Ti–15Si samples meltpool boundaries were far less prominent (Figure 4 b, j and k). While significant cracking was observed in the single line scan melt pools of the Ti–15Si sample, no cracking was observed in the full surface remelt. Large silicides in the arc-melted region did exhibit cracking, but this cracking did not propagate through the melt pool. Conversely, while the single line scan melt pools of the Ti–32.5Fe sample remained intact with cracking in the arc-melted region, significant repeated cracking was observed in the full surface remelt region (Figure 5).

All samples demonstrated a significant increase in hardness values within the laser remelt regions. The hardness is noted to increase with alloying addition, with the exception that the eutectic composition Ti–8.5Si wt-% exhibited superior hardness to the hypereutectic Ti–15Si wt-% composition (Table 1).

## *APT*

The APT reconstruction, Figure 6, illustrates the cellular-dendritic nanostructure from the Ti–15Si wt-% laser remelt region. It reveals interconnectivity of both the Si-rich and Ti-rich phases, and a tendency to form parallel plates. The characteristic length scale is approximately 20 nm. The proxigram concentration profile (in at.-%) across the interface between the Ti-rich and Si-rich phases confirms the cellular structure consists of Ti ( $\sim$ 98.4 at.-%) with an inter-cellular region of titanium silicide with $\sim$ 30.1 –34.5 at.-%) Si (Figure 7). Close to the interface, the Si concentration goes through a maximum at 34.5 at.-% before reaching a far-field

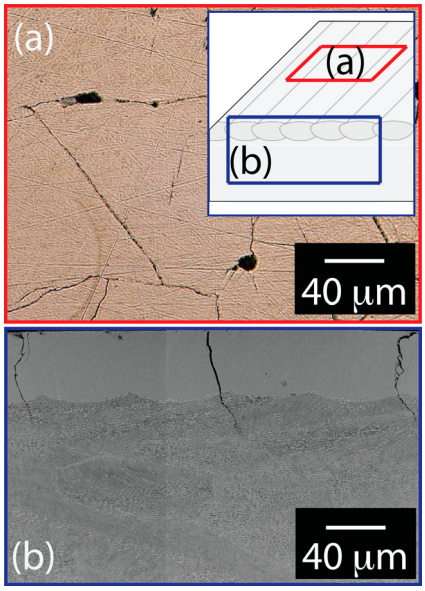


**Figure 5.** (a) Optical micrograph of the surface remelt, and (b) secondary electron SEM imaging of the sectioned surface normal to the surface remelt of Ti–32.5Fe, with cracking clearly visible Rastering path was vertical with regard to optical microscopy image (a).

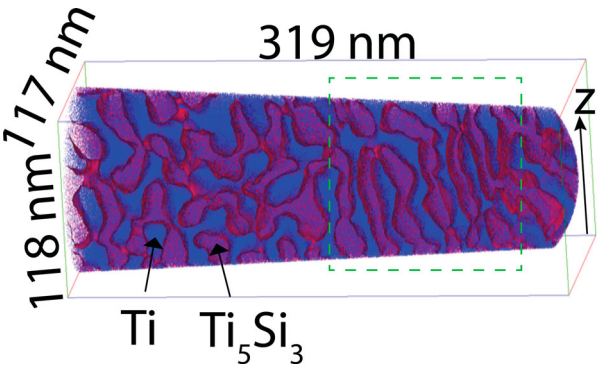


**Figure 6.** Ti–15Si wt-% sample: APT atom-by-atom reconstruction of a volume in the laser remelt region targeted by FIB lift-out preparation. To highlight the titanium silicide phase, an isoconcentration surface at the 25.0 at.-% Si level is superposed. Only 2.5% of Ti (blue) and 5% of Si (red) atoms are shown for clarity. A green box highlights alignment relative to the laser scanning direction indicated by the arrow with label 'z'.

plateau concentration of about 30.1 at.-%. The atomic fraction of the silicide phase can be evaluated from the APT reconstruction by counting the number of atoms in the silicide, relative to the total number of atoms in the reconstruction volume. To sensibly threshold the boundary between the two phases, an isoconcentration threshold is selected at 18 at.-% Si, representing the midpoint concentration between the plateau concentration of the Ti-rich phase at 1.6 at.-% Si, and the maximum Si concentration in the silicide at 34.5 at.-%. This process results in an atomic fraction of 49.5 at.-% titanium silicide, representative of the volume fraction under the assumption that the effective atomic volume is similar in both phases.

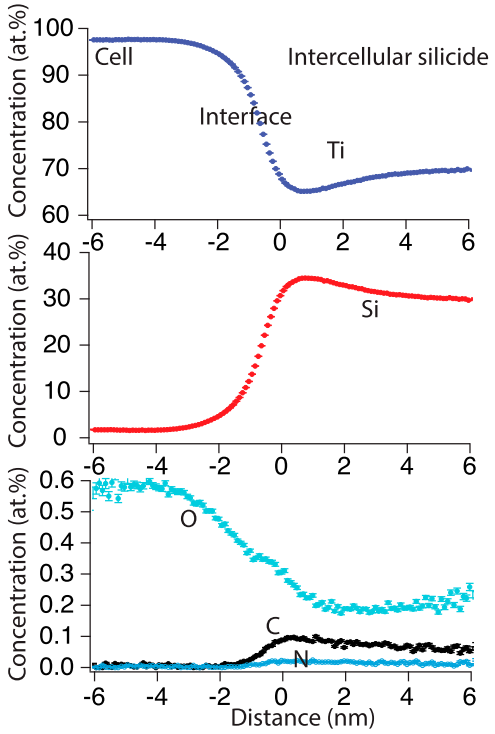


**Figure 7.** Proximity histogram concentration profiles (in at.-%) across the interface between Ti-rich cells and intercellular silicides for Ti–15 wt-% Si (23.5 at.-%) sample following a laser remelt linescan at 140 W/800 mm $s^{-1}$ laser pulse. Proxigram calculated with respect to a 25 at.-% Si isoconcentration surface.

## Discussion

### *Phase stability*

The Ti–B and Ti–C phase diagrams are uncertain in many aspects, and disagreement regarding the eutectic composition exists in the literature [27–29]. B and C rapidly partition to grain boundaries, and Ti readily absorbs O and N which are known to cause pronounced changes in phase diagrams and mechanical properties. The eutectic compositions defined herein, 1.5 at.-% C and 7 at.-% B, were chosen as target nominal compositions as they were experimentally derived from a multi-technique investigation [43] and agree with subsequent thermodynamic assessments [27, 28, 44]. Regarding the Ti–Si phase diagram, the stability of $Ti_3Si$ on the Ti-rich side is debated [45], however, it has been observed in a number of alloys following multi-step heat-treatments [46]. The ambiguity is again likely due to the affinity of Ti alloys for oxygen, which modifies phase equilibria [47].

### *SEM*

High-resolution SEM imaging was performed for all samples, and notable microstructural differences were observed. The nanostructure of Ti–0.38C wt-% was nanocellular with nanoliths (Figure 8 a). This is in contrast to the laser remelt nanocellular structure of the Ti–1.67B wt-% which exhibits an absence of nanoliths

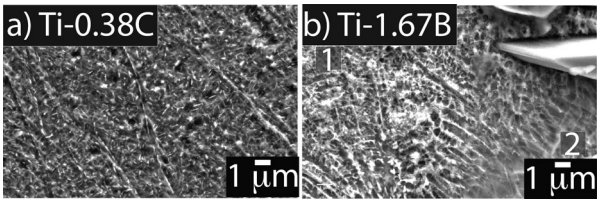


**Figure 8.** Secondary electron SEM images of 140 W laser energy laser remelt regions for (a) Ti–0.38C wt-% and (b) Ti–1.67B wt-% alloys. Figure (b) illustrates the interface region.

(Figure 8b). This may be associated with the difference in interstitial additions. The nanolath morphology within the Ti–0.38C wt-% sample resembles that of acicular $\alpha'$, but more advanced characterisation techniques are required to be conclusive. It was qualitatively noted that, for all laser remelt nanocellular structures, the cell size was greatest at the interface region between laser remelt and arc-melted zones (zone 2 in Figure 8(b)), and decreased in size towards the center of the laser remelt region (zone 1).

The Ti–8.5Si wt-% presented a uniform nanocellular structure throughout the melt pools with a directionality aligned with the thermal gradient (Figure 9 a). A zone of lamellar nanostructure typical of eutectic composition phase separation is observed at consecutive melt pool interfaces (Figure 9 b). The Ti–15Si wt-% sample microstructure differed between the single line scan and the full surface remelt, where the single line scan melt pools exhibited significant variation in the distribution of silicide precipitates and nanocellular or lamellar microstructures, Figure 9(c) and 9(d), compared to the full surface remelt exhibiting a more even distribution of microscale silicide precipitates within a nanoprecipitate containing matrix (Figure 9 e and 9f). These differences may be explained as a function of the successive, overlapping remelting process providing for diffusion of the hypereutectic composition compared to the single line scans operating on arc-melted sample containing silicide precipitates sized on the order of the melt pool cross section itself.

Ti–32.5Fe wt-% possessed a directional lamellar structure with a sharp interface between the arc-melted region and the laser remelt region (Figure 10 a). The thermal conductivity (at room temperature and 1 bar) of pure Fe (80 W/m°C) is approximately three times higher than that of commercially pure Ti (17 W/m°C) [48]. The expected higher growth rate (based on the relatively higher thermal conductivity) must therefore be balanced by the high thermal gradient in the laser remelt environment to present columnar grains of phase stabilised $\beta$-titanium and TiFe.

### *XRD*

The Bragg–Brentano XRD is a surface analysis technique, and the current work applies this technique

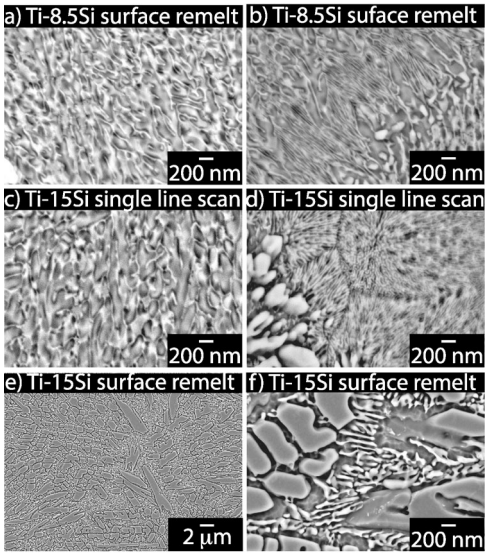


**Figure 9.** High magnification secondary electron SEM images illustrating (a) the broadly consistent nanocellular structure of the laser remelted surface of the Ti–8.5 wt-% sample, and (b) the lamellar eutectic structure at the melt pool overlap of the same sample; (c) nanocellular structure found in the single line scans of the Ti–15Si wt-% sample, and (d) nanoscale lathe structure adjacent to silicide precipitates; compared to (e) the more evenly diffused silicide precipitates of the full surface melt Ti–15Si wt-% sample, with (f) showing silicide precipitates with a lathe microstructure matrix.

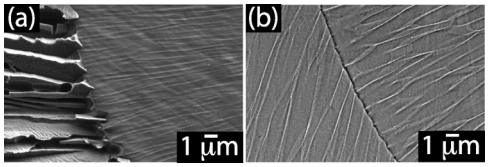


**Figure 10.** Secondary electron SEM images of the Ti–32.5Fe wt-% sample illustrating (a) the single line scan melt pool to arc-melt interface, and, (b) the full surface remelt melt pool overlap interface. Note the directionally oriented lamellar microstructure.

to characterise the phases within laser remelt surface scans. The X-ray penetration depths were calculated from the data of Henke et al. [49] and presented for pure Ti and Ti–32.5Fe wt-% (Figure 11), where the change of penetration depth to pure Ti with the additions of Si, B and C additions is negligible. The informative diffraction peaks from the XRD patterns are contained below $2\theta = 45°$ (Figure 1), and referring to the penetration depth calculation it is reasonable to conclude that the bulk of the diffracted intensity is from the laser remelt layer in the samples. This is further reinforced by the total $\alpha$ to $\beta$ phase transformation observed in the laser remelt pattern of Ti–32.5Fe wt-%, where probing the arc-melted region + laser remelt region would have resulted in the observation of $\alpha$ phase reflections.

In the current work, given the nano length-scales and that SEM-EDX is not suitable for C and B analysis, it is not possible to distinguish between $\alpha'$ or TiC nanolaths from XRD and SEM (Figures 1 a and 8a),

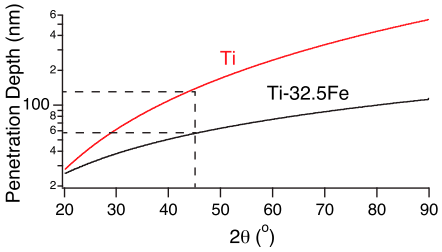


**Figure 11.** Calculated lab X-ray penetration depth at 20keV for Ti and Ti–32.5Fe.

particularly given the low solubility of C in Ti and the uncertainty regarding the eutectic composition. There is no evidence of $\alpha'$ in the Ti–B SEM (Figure 8 a), and based on the similarity of the nanostructure to the Ti–Si APT specimen (Figure 6), it is reasonable to conclude that the microstructure is composed of $\alpha$ Ti cells with TiB cell boundaries, which is informed by XRD (Figure 8 b).

The diffraction peaks of the Ti–15Si wt-% alloy from the LPBF surface are more distinct than those of the Ti–8.5Si wt-% alloy (Figures 1 c and 1e), associated with the larger precipitates in the hyper-eutectic composition (Figure 9 b). From the rapid cooling rates associated with laser remelting and based on the diffraction patterns, we conclude that the alloys are composed of $\alpha$-Ti + $Ti_5Si_3$, where lower temperature phase transformation to $Ti_3Si$ would require low temperature holds to achieve sufficient diffusion. This is confirmed subsequently by APT.

Fe is the strongest $\beta$-stabilising element, requiring just 3.5 wt-% to retain 100% of the bcc $\beta$-phase on quenching to room temperature [50]. It is clear from the laser remelt XRD pattern of Ti–32.5Fe wt-% (Figure 9d) and the SEM (Figure 9d) that we have achieved a directional composite nanograin structure of $\beta$-Ti +TiFe aligned towards the melt-pool center.

## APT

The APT 3D reconstruction in Figure 6 reveals a cellular-dendritic structure clearly related to a eutectic solidification reaction during cooling of the alloy after melting during the laser line scan, with the characteristic spacing of the reaction products of approximately 20 nm related to and caused by the high cooling rate. A nano-scale two-phase structure with a high volume fraction (49.5 at.-% titanium silicide) of the ceramic phase in a Ti–metal matrix of about 51.5 at.-% is desirable in terms of enhancing alloy strength. The reaction proceeds by forming a cellular-dendritic interconnected structure, occasionally with a tendency to form parallel nano-scale plates which would be expected from a eutectic reaction during solidification producing a Ti-rich and a silicide phase. The green box in Figure 6 highlights the plate-like morphology with an alignment that is compatible with an eutectic reaction front moving along the direction of overall heat flow during the fast cooling, that is the direction parallel to the LPBF 'build' direction, indicated by the arrow with label 'z' in Figure 6.

The phase compositions measured by APT are compatible with the XRD results for the crystallographic structures present, that is $\alpha$-Ti with 1.1 wt-%Si (1.6 at.-%) and $Ti_5Si_3$ with 20.2 wt-%Si (30.1 at.-%) in the plateau region of the proxigram (Figure 7) and 23.1 wt-% (34.5 at.-%) in the region with the maximum Si concentration close to the interface. These concentrations are consistent with a metastable supersaturated $\alpha$-Ti phase and a Si-depleted $Ti_5Si_3$ phase. Following reference [45], the $Ti_5Si_3$ phase is the only intermetallic phase in the binary Ti–Si system that has an extended concentration range (all other intermetallic phases are line compounds) indicating that $Ti_5Si_3$ structure can accommodate non-stoichiometric compositions. After rapid solidification, a residual supersaturation would be expected and that seems to be the case for both the $\alpha$-Ti and $Ti_5Si_3$ phase. The maximum in Si concentration at 23.1 wt-% (34.5 at.-%) observed close to the interface could be related to a supersaturated $\alpha$-Ti solid solution expelling Si during the cooling at lower temperatures that is then observed as a Si *bump* with higher concentration in the surface region of the $Ti_5Si_3$ phase (Figure 7). The proxigram also shows that the $\alpha$-Ti-stabilising elements O (0.6 at.-%) and H (0.1 at.-%) are enriched in $\alpha$-Ti, but not N and C which are enriched in the $Ti_5Si_3$ phase at 0.01 at.-% N and 0.06 at.-%C. Tracking impurity concentrations is important for Ti alloys where specifically oxygen is (i) present in significant concentrations after standard processing and is (ii) known to affect the phase relations and equilibria in Ti alloys.

The overall composition of the volume captured by the APT run is 17.8 at.-% (11.3 wt-%) Si, a hypereutectic composition relative to the equilibrium eutectic point at 13.7 at.-% (8.5 wt-%) [45]. This composition is lower than the nominal 15 wt-% Si of the arc-melted alloy but may be related to the formation of large silicide particles as mentioned above which would reduce the Si concentration in the remaining alloys sample. If this is the composition inherited from the melt, the eutectic solidification likely proceeds by first forming silicide crystallites and pockets (cells) with supersaturated liquid Ti that subsequently solidify to form alpha-Ti with a low silicon solubility.

## Hardness tests

The laser remelt hardness tests (Table 1) illustrate the following approximate conclusions: a) 0.4 wt-% C addition increases the laser remelt hardness (455 Hv) by 160% compared to laser remelt of pure Ti (175 Hv), while 1.6 wt-% B addition increases the hardness

(465 Hv) by about 165%. 8.5 wt-% addition of Si increases the hardness by 290% (685 Hv), and 32.5 wt-% Fe increases the hardness by 340% (770 Hv). These high micro-hardnesses are noteworthy, for comparison, an optimised $\beta$-Ti alloy reinforced by nanoscale $\alpha$ precipitates typically achieve high hardnesses around 500 Hv [51]. Thus this hardness is exceeded with Si and Fe eutectic composition additions.

### *Summary and comparison to archival literature*

Historically, poor processability was the primary limiting factor regarding Ti MMC development, thus it is encouraging that the eutectic composition alloys show amenability to LPBF. $Ti_5Si_3$ possesses a highly anisotropic thermal expansion coefficient that is poorly matched to Ti alloys, [52–54] which would create additional shrinkage strain within the melt pool itself. This may explain the significant cracking of the single line scan hypereutectic Si alloy where the arc-melted medium contained very large silicide precipitates, which was not observed within the other alloy compositions.

There are multiple factors that make eutectic Ti–Fe materials processed via LPBF of interest, including enhanced processability on account of the $\beta$-Ti phase, higher strength (evidenced by the hardness values in Table 1) and the potential for ductility in a more coherent nanostructure within LPBF regions [55]. It is particularly noteworthy that cracking was observed within the arc-melted region following single line scan remelting, Figure 3, and throughout the full surface remelt region without lateral cracking through the arc-melted region, Figure 5, indicating major shrinkage strain inherent to the rapid cooling and $\beta$-Ti phase stabilisation. Further development of scanning parameters may balance the stresses involved to eliminate cracking in full surface remelting.

Ti–32.5Fe alloys have previously been LPBF fabricated from powder blends by Gussone et al., utilising a heated plate for the LPBF process [9]. The reported microstructures are very different to those reported herein, and these differences are not simply due to the difference in LPBF conditions. In their study, insufficient mixing of Ti and Fe resulted in a considerable fraction of $\alpha$-Ti regions as well as Fe rich areas, while oxygen contamination produced $\eta$-$Ti_4Fe_2O_x$ and a cellular dendritic microstructure. This is in stark contrast to the directional lamellar microstructure found herein (Figure 10).

In summary, Ti–Si is a desirable material when considering high strength-to-weight ratio and the initial research presented herein suggests potential amenability to full LPBF. The Ti–Fe eutectic system are also promising for future LPBF alloys. It has extremely high hardness, is composed of directional nano-grains, and high Fe addition will lower the cost of the Ti alloy substantially. Processability of Ti–Fe alloys may be enhanced with further alloying, but this hypothesis requires further research. The interstitial element eutectic alloys are also promising, but require further alloying to increase hardness. Thus, the base alloys have been assessed and presented, and warrant further research particularly regarding multi-component alloys and ductility, where bulk ductility measurements necessitate powder fabrication.

## Conclusion

The following primary conclusions are drawn:

- Binary Ti–0.38C wt-%, Ti–1.67B wt-% and Ti 8.5Si wt-% eutectic composition all exhibit potential amenability to LPBF, while Ti–32.Fe wt-% suffered from cracking on surface remelting.
- Extensive cracking was observed in single line scan laser remelting of a hyper-eutectic Ti–15Si wt-% alloy, associated with large silicides that nucleate during cooling from liquidus to solidus.
- The nanostructures are cellular in the C, B and Si containing alloys, but directionally grained for the Ti–Fe alloy. The cell boundaries are composed of boride/carbide/silicide. The difference in nanostructure can be associated with the lower thermal conductivity of Fe relative to Ti and the high concentration of Fe addition.
- Fe is a $\beta$ stabiliser and the $\beta$ to $\alpha$ phase transformation is fully suppressed under LPBF conditions in the Ti–Fe alloy considered.
- The Si and Fe containing materials exhibited hardnesses that greatly exceed conventional high-strength $\beta$-Ti alloys.
- Further mechanical property assessment will require powder fabrication. This will enable detailed assessment of alloy ductility, which is a traditional concern regarding MMCs. A high concentration of Fe addition will lower material cost and provide high hardness, but increase density. Conventional $\beta$-Ti alloy properties are highly tunable based on alloy additions, making Ti–Fe based alloys fabricated via LPBF a candidate for materials advancement despite initial cracking concerns in the binary eutectic system. Ti–Si alloys are highly desirable based upon the high hardness and low density composition, and the binary system appears to be processable via LPBF in this work. Finally, limited B and C additions dramatically increase hardness compared to pure Ti, making them suitable candidate systems warranting further development.

From the systematic review of four binary Ti-based MMCs above, it appears that MMCs fabricated via LPBF have the potential to outperform conventional alloys.

## Acknowledgments

We are grateful for the assistance and support of Dr. Chip Tomonto, Dr. Colton Steiner, Dr. Nader Dariavach and Mr. Jorge Alvarez in facilitating our research at The UM College of Engineering – Johnson & Johnson 3D Printing Center of Excellence Collaborative Laboratory and for performing the laser powder bed fusion. Atom-probe tomography was performed at the Northwestern University Center for Atom-Probe Tomography (NUCAPT).

## Disclosure statement

No potential conflict of interest was reported by the author(s).

## Funding

The LEAP tomograph at NUCAPT was purchased and upgraded with grants from the NSF-MRI (DMR-0420532) and ONR-DURIP (N00014-0400798, N00014-0610539, N00014-0910781, N00014-1712870) programs. NUCAPT received support from the MRSEC program (NSF DMR-1720139) at the Materials Research Center, the SHyNE Resource (NSF ECCS-2025633), and the Initiative for Sustainability and Energy (ISEN) at Northwestern University. ICP-OES was performed by Matexcel.

## Data availability

Data are available at doi:10.17632/st3zbsnrc6.1

## ORCID

*James Coakley* http://orcid.org/0000-0001-8721-0438

## References

[1] Miracle DB Opportunities and approaches for doubling the structural efficiency of metallic materials. In *Metallic Materials with High Structural Efficiency*; Springer; 2004. p. 3–20.
[2] Vardiman RG, Kant RA. The improvement of fatigue life in Ti–6Al–4V by ion implantation. J Appl Phys. 1982;53(1):690–694.
[3] Ralph B, Yuen HC, Lee WB. The processing of metal matrix composites–an overview. J Mater Proces Technol. 1997;63(1-3):339–353.
[4] Dadbakhsh S, Mertens R, Hao L, et al. Selective laser melting to manufacture "in situ" metal matrix composites: a review. Adv Eng Mater. 2019;21(3):1801244.
[5] Shi J, Wang Y. Development of metal matrix composites by laser-assisted additive manufacturing technologies: a review. J Mater Sci. 2020;55(23):9883–9917.
[6] Liu S, Shin YC. The influences of melting degree of tic reinforcements on microstructure and mechanical properties of laser direct deposited Ti6Al4V-tic composites. Mater Des. 2017;136:185–195.
[7] Euh K, Lee J, Lee S. Microstructural modification and property improvement of boride/Ti–6Al–4V surface-alloyed materials fabricated by high-energy electron-beam irradiation. Metall Mater Trans A. 2001;32(10):2499–2508.
[8] Attar H, Bönisch M, Calin M, et al. Selective laser melting of in situ titanium–titanium boride composites: processing, microstructure and mechanical properties. Acta Mater. 2014;76:13–22.
[9] Gussone J, Bugelnig K, Barriobero-Vila P, et al. Ultrafine eutectic Ti–Fe-based alloys processed by additive manufacturing–a new candidate for high temperature applications. Appl Mater Today. 2020;20:100767.
[10] Cai C, Radoslaw C, Zhang J, et al. In-situ preparation and formation of Tib/Ti–6Al–4V nanocomposite via laser additive manufacturing: microstructure evolution and tribological behaviour. Powder Technol. 2019;342:73–84.
[11] Wei W, Zhang Q, Wu W, et al. Agglomeration-free nanoscale tic reinforced titanium matrix composites achieved by in-situ laser additive manufacturing. Scr Mater. 2020;187:310–316.
[12] Pouzet S, Peyre P, Gorny C, et al. Additive layer manufacturing of titanium matrix composites using the direct metal deposition laser process. Mater Sci Eng A. 2016;677:171–181.
[13] Dadbakhsh S, Mertens R, Vanmeensel K, et al. In situ transformations during SLM of an ultra-strong tic reinforced ti composite. Sci Rep. 2020;10(1):1–12.
[14] Zhang L-C, Attar H. Selective laser melting of titanium alloys and titanium matrix composites for biomedical applications: a review. Adv Eng Mater. 2016;18(4):463–475.
[15] Fang M, Han Y, Shi Z, et al. Embedding boron into ti powder for direct laser deposited titanium matrix composite: microstructure evolution and the role of nano-tib network structure. Compos Part B: Eng. 2021;211:108683.
[16] Huang L, An Q, Geng L, et al. Multiscale architecture and superior high-temperature performance of discontinuously reinforced titanium matrix composites. Adv Mater. 2021;33(6):2000688.
[17] Fereiduni E, Ghasemi A, Elbestawi M. Selective laser melting of hybrid ex-situ/in-situ reinforced titanium matrix composites: laser/powder interaction, reinforcement formation mechanism, and non-equilibrium microstructural evolutions. Mater Des. 2019;184:108185.
[18] Patil AS, Hiwarkar VD, Verma PK, et al. Effect of tib2 addition on the microstructure and wear resistance of Ti–6Al–4V alloy fabricated through direct metal laser sintering (dmls). J Alloys Compd. 2019;777:165–173.
[19] Chen G, Liu R-Z, Qiu Y-D, et al. Effect of laser parameters on microstructure and phase evolution of Ti–Si–C composites prepared by selective laser melting. Mater Today Commun. 2020;24:101114.
[20] He Y, Montgomery C, Beuth J, et al. Melt pool geometry and microstructure of ti6al4v with b additions processed by selective laser melting additive manufacturing. Mater Des. 2019;183:108126.
[21] Mathers G. The welding of aluminium and its alloys. Woodhead Publishing; 2002.
[22] Sabzi HE, Rivera-Díaz-del Castillo PE. Defect prevention in selective laser melting components: compositional and process effects. Materials. 2019;12(22):3791.
[23] Lu L, Nogita K, McDonald SD, et al. Eutectic solidification and its role in casting porosity formation. JOM. 2004;56(11):52–58.
[24] Alagarsamy A, Kumar S. Demystifying shrinkage porosity in ductile iron castings. Int J Metalcasting; 2020. p. 1–16.
[25] Vrancken B, King WE, Matthews MJ. In-situ characterization of tungsten microcracking in selective laser melting. Procedia CIRP. 2018;74:107–110.

[26] Sustarsic B, Dolinsek S, Jenko M, et al. Microstructure and mechanical characteristics of DMLS tool-inserts. Mater Manuf Proces. 2009;24(7-8):837–841.
[27] Seifert HJ, Lukas HL, Petzow G. Thermodynamic optimization of the Ti–C system. J Phase Equilibria. 1996;17(1):24–35.
[28] Uhrenius B. Calculation of the Ti–C, Wc and Ti–Wc phase diagrams. Calphad. 1984;8(2):101–119.
[29] Murray JL, Liao PK, Spear KE. The B- ti (boron-titanium) system. Bull Alloy Phase Diagr. 1986;7(6):550–555.
[30] Sabooni S, Karimzadeh F, Abbasi MH. Thermodynamic aspects of nanostructured $ti_5Si_3$ formation during mechanical alloying and its characterization. Bull Mater Sci. 2012;35(3):439–447.
[31] Contieri RJ, Lopes ESN, Taquire de La Cruz M, et al. Microstructure of directionally solidified ti–fe eutectic alloy with low interstitial and high mechanical strength. J Cryst Growth. 2011;333(1):40–47.
[32] Coakley J, Radecka A, Dye D, et al. Characterising nanoscale precipitation in a titanium alloy by laser-assisted atom probe tomography. Mater Charact. 2018;141:129–138.
[33] Thompson K, Lawrence D, Larson DJ, et al. In situ site-specific specimen preparation for atom probe tomography. Ultramicroscopy. 2007;107(2–3):131–139.
[34] Kelly TF, Larson DJ. Local electrode atom probes. Mater Charact. 2000;44(1-2):59–85.
[35] Hellman OC, Vandenbroucke JA, Rüsing J, et al. Analysis of three-dimensional atom-probe data by the proximity histogram. Microsc Microanal. 2000;6(5):437–444.
[36] Hellman OC, Rüsing J, Sebastian JT, et al. Atom-by-atom chemistry of internal interfaces: simulations and experiments. Mater Sci Eng C. 2001;15(1-2):13–15.
[37] Hellman O, Vandenbroucke J, Du Rivage JB, et al. Application software for data analysis for three-dimensional atom probe microscopy. Mater Sci Eng A. 2002;327(1):29–33.
[38] Hellman OC, Du Rivage JB, Seidman DN. Efficient sampling for three-dimensional atom probe microscopy data. Ultramicroscopy. 2003;95:199–205.
[39] Isheim D, Hellman OC, Rüsing J, et al. Atomic-scale structure and chemistry of segregation at matrix/ precipitate heterophase interfaces. Interface Sci. 2001;9(3):257–264.
[40] Jain A, Ong SP, Hautier G, et al. The materials project: A materials genome approach to accelerating materials innovation. APL Mater. 2013;1(1):011002. ISSN 2166532X. doi:10.1063/1.4812323
[41] Niinomi M. Low-modulus ti alloys suitable for rods in spinal fixation devices. In: Sasaki K, Suzuki O, and Takahashi N, editors. Interface Oral Health Science 2016. Singapore: Springer; 2017. p. 3–21. ISBN 978-981-10-1560-1.
[42] Coakley J, Vorontsov VA, Littrell KC, et al. Nanoprecipitation in a beta-titanium alloy. J Alloys Compd. 2015;623:146–156. ISSN 0925-8388. doi:10.1016/j.jallcom.2014.10.038
[43] Rudy E, Windisch S. Ternary phase equilibria in transition metal–boron–carbon–silicon systems. part i. related binary system, technical report no. afml-tr-65-2, 1966.
[44] Ma X, Li C, Du Z, et al. Thermodynamic assessment of the Ti–B system. J Alloys Compd. 2004;370(1-2):149–158.
[45] Massalski TB, Murray JL, Bennett LH. Binary alloy phase diagrams materials park. Ohio: ASM-International; 1990.
[46] Bulanova M, Firstov S, Kulak L, et al. Multicomponent Ti–Si-based systems. In Metallic Materials with High Structural Efficiency; Springer; 2004. p. 217–228.
[47] Salpadoru NH, Flower HM. Phase equilibria and transformations in a Ti–Zr–Si system. Metall Mater Trans A. 1995;26(2):243–257.
[48] Carvill J. 3 – thermodynamics and heat transfer. In: Carvill J, editor, Mechanical Engineer's Data Handbook; Oxford: Butterworth-Heinemann; 1993. p. 102–145. ISBN 978-0-08-051135-1. Doi:10.1016/B978-0-08-051135-1.50008-X
[49] Henke BL, Gullikson EM, Davis JC. X-ray interactions: photoabsorption, scattering, transmission, and reflection at e = 50-30,000 ev, z = 1-92. At Data Nucl Data Tables. 1993;54(2):181–342. ISSN 0092-640X. doi:10.1006/adnd.1993.1013
[50] Kolli RP, Devaraj A. A review of metastable beta titanium alloys. Metals. 2018;8(7):506.
[51] Coakley J, Vorontsov VA, Jones NG, et al. Precipitation processes in the beta-titanium alloy Ti–5Al–5Mo–5V–3Cr. J Alloys Compd. 2015;646:946–953. ISSN 0925-8388. doi:10.1016/j.jallcom.2015.05.251
[52] Frommeyer G, Rosenkranz R. Structures and properties of the refractory silicides Ti 5 Si 3 and TiSi 2 and Ti–Si–(Al) eutectic alloys. In Metallic materials with high structural efficiency; Springer; 2004. p. 287–308.
[53] Lütjering G, Williams JC. Titanium. Springer Science & Business Media; 2007.
[54] Schneibel JH, Rawn CJ. Thermal expansion anisotropy of ternary titanium silicides based on $ti_5Si_3$. Acta Mater. 2004;52(13):3843–3848.
[55] Zhong Y. Sub-grain structure in additive manufactured stainless steel 316L [dissertation]. Department of Materials and Environmental Chemistry, Stockholm University; 2017.